IOP Publishing Biomed. Mater. 17 (2022) 035008 https://doi.org/10.1088/1748-605X/ac6471

Biomedical Materials

PAPER

RECEIVED
13 January 2022

REVISED
29 March 2022

ACCEPTED FOR PUBLICATION
5 April 2022

PUBLISHED
19 April 2022

3D printed hydroxyapatite promotes congruent bone ingrowth in rat load bearing defects

Juhi Chakraborty, Subhadeep Roy and Sourabh Ghosh*

Department of Textile and Fibre Engineering, Indian Institute of Technology, Delhi, Hauz Khas, New Delhi, India
* Author to whom any correspondence should be addressed.

E-mail: sghosh08@textile.iitd.ac.in

Keywords: 3D printing, hydroxyapatite, *in vivo*, rat bone, load-bearing defect, tibia

Abstract

3D porous hydroxyapatite (HAP) scaffolds produced by conventional foaming processes have limited control over the scaffold's pore size, geometry, and pore interconnectivity. In addition, random internal pore architecture often results in limited clinical success. Imitating the intricate 3D architecture and the functional dynamics of skeletal deformations is a difficult task, highlighting the necessity for a custom-made, on-demand tissue replacement, for which 3D printing is a potential solution. To combat these problems, here we report the ability of 3D printed HAP scaffolds for *in vivo* bone regeneration in a rat tibial defect model. Rapid prototyping using the direct-write technique to fabricate 25 mm^2 HAP scaffolds were employed for precise control over geometry (both external and internal) and scaffold chemistry. Bone ingrowth was determined using histomorphometry and a novel micro-computed tomography (micro-CT) image analysis. Substantial bone ingrowth was observed in implants that filled the defect site. Further validating this quantitatively by micro-CT, the Bone mineral density (BMD) of the implant at the defect site was 1024 mgHA ccm^{-1}, which was approximately 61.5% more than the BMD found with the sham control at the defect site. In addition, no evident immunoinflammatory response was observed in the hematoxylin and eosin micrographs. Interestingly, the present study showed a positive correlation with the outcomes obtained in our previous *in vitro* study. Overall, the results suggest that 3D printed HAP scaffolds developed in this study offer a suitable matrix for rendering patient-specific and defect-specific bone formation and warrant further testing for clinical application.

1. Introduction

Extensive efforts have been directed towards fabricating a suitable biomaterial scaffold as a bone substitute for critical bone defects. Scientists were in an unrestrained bout to develop materials that offer the potential to support the osteogenic differentiation of osteoprogenitor cells along with mineralization [1], toughness matching mechanical properties of bone, osteogenic signaling [2], the ability to remodel mineralized matrix *in vivo,* controlled biodegradation, and long-term sustainability [3]. Of the wide variety of advanced materials and the associated therapies, only a handful could achieve debatable success in pre-clinical *in vivo* trials. A multicenter study to critically analyze the effect of 93 different biomaterials, 47 *in vitro* studies, and 36 *in vivo* studies highlighted poor correlation between *in vitro* and *in vivo* assessments of osteoinductive biomaterials in small and large animals models [4]. This disappointing correlation indicates an urgent need for more systematic *in vitro* assays and more well-defined *in vivo* trials in animal models. To resolve this problem, a combinatorial approach involving suitable biomaterials and *in vitro* osteogenic differentiation protocol should be pursued, recapitulating developmental biology aspects for the differentiation of osteoblasts via endochondral ossification. Matching gene expression trajectories *in vitro* and *in vivo* would help generate deep mechanistic insights into the signaling pathways involved in bone formation [5].

At present, bone autografts and allografts are considered the gold standard for treating bone defects [6]. However, several drawbacks are associated with the use of autologous bone grafts, which limit their application, including a high rate of graft resorption, donor site morbidity, and constrained availability [7, 8]. Although allografts can overcome some of these drawbacks, they are also constrained by certain factors, such as decreased bioactivity and strength due to processing and decreased integration with the native tissue [9]. In addition, readily available metal implants have been employed to address bone defects. Despite their ability to eliminate the possibility of disease transmission from the donor to the host, they can elicit an immune response leading to graft failure and stress shielding, which may demand additional surgeries [10]. This has resulted in the commercialization of a range of osteoconductive ceramics and bioactive glasses [11] for bone regeneration in clinical settings. While these materials provide an osteoconductive platform for bone growth, clinical success is limited as the materials fail in cases of complex skeletal deformations and critical-sized injuries. The reasons were multifactorial: (a) commercial osteogenic materials were available in standard shapes and sizes and hence could not match the complexity of individual patient defects; (b) the materials had to be reshaped intraoperatively by clinicians, a method prone to human errors, and (c) disparity in the biomechanical stresses of different regions of the skeleton cannot be cured using standard materials. Therefore, a detailed systematic study with a sheer focus on all the essential parameters and their careful evaluation can help fabricate a suitable 3D biomimetic scaffold for bone tissue engineering.

Bone is a diverse complex material consisting of a blend of hydroxyapatite (HAP) [12] and sorted organic components constituting type I collagen, lipids, and non-collagenous proteins [13]. Hence, it would be rational to explore these components for the fabrication of an appropriately designed scaffold that is likely to impart enhanced scaffold bioactivity and structural biomimicry. This would ultimately aid in enhanced osteoconduction (ingrowth and proliferation of osteoblasts of osteoprogenitors), osseointegration (scaffold anchorage to host bone tissue) [14], osteoinduction (development of immature host cells to osteogenic cells) [15] and increased vascularization [16]. In this context, HAP has been widely explored as a scaffold for bone tissue engineering owing to its outstanding properties and its potential to serve as a temporary framework to aid in bone remodeling [17, 18]. Moreover, its compositional resemblance with bone and the ability of the HAP constructs to form a robust bond with the surrounding bone has bestowed it to become the scaffold of choice by most bone tissue engineers [17]. However, it shares some standard features with other ceramics, including brittleness and rigidness, limiting HAP constructs' effectiveness for load-bearing and their molding into shapes specific to bone defects.

Three-dimensional (3D) printing or rapid prototyping technology is the most efficacious approach for simulating complex native bone structures for designing patient-specific grafts using clinical images (CAT scan or MRI). An increasing number of tissue engineering studies advocate the use of 3D printed scaffolds made of ceramics and osteoinductive materials (HAP, bioactive glass composites, decellularized bone matrix) fabricated through a diverse number of methods that aid in bone regeneration. Among the osteoinductive materials mentioned above, HAP is primarily used in powder form as bone fillers [19] or 3D porous scaffolds [20]. 3D printed HAP scaffolds with a broad distribution of randomly connected pores aid tissue ingrowth and augment bone regeneration [21]. HAP scaffolds produced by fused deposition or stereolithography necessitate long heating cycles to eliminate organic species without introducing defects successfully. Michna *et al* [22] developed a concentrated HAP ink with optimized viscoelastic characteristics for direct-write assembly (DWA) of multiscale porosity 3D periodic scaffolds. The scaffolds can be rapidly heated after drying because the ink contains low organic species (1%–2% by volume). In this method, the ink is continually extruded in a filamentary form in a layer-by-layer build sequence to generate the appropriate scaffold structure. This technique permits accurate control over the location and size of the printed filament within each scaffold. Interestingly, these printed scaffolds aid in the growth of human bone marrow-derived mesenchymal stem cells to analyze the *in vitro* emergence of the mineral-enriched construct [23]. Although the surgical procedures involving scaffold implantation are highly significant, these clinical ventures become successful only when the osteoprogenitor cells from the neighboring bone migrate to the implant site, followed by the deposition of protein forming a non-mineralized matrix. Calcification of this matrix along with the formation of pre-osteocytes from the osteoblasts, followed by their conversion into terminally differentiated and mineral-producing osteocytes, resulting in enhanced osseointegration [24, 25].

Recent studies have elucidated that HAP, when used in the form of a nanocomposite, augmented the expression of osteogenic proteins alkaline phosphate (ALP), osteocalcin (OC), and osteopontin (OPN), along with enhanced calcium deposition, which is involved in osteogenic differentiation and mineralization [26]. This is in accordance with the findings of Martinelli *et al* [27]. They reported increased OC and OPN activity while using nanohydroxyapatite carbon composites; increased ALP activity was observed, which showed the potential of the nanohydroxyapatite to enhance biomineralization. In comparison to these studies, in our previous study, we demonstrated that 3D printed HAP scaffolds could regulate the

differentiation of osteocytes in contrast to 2D HAP scaffolds. The unique finding of our study was that 3D HAP scaffolds printed via DWA were able to modulate the complex process involving the formation of the osteocyte-like phenotype by the differentiation of osteoblasts. This was successfully achieved primarily because of the 3D architecture of the scaffold, surface roughness, and stiffness, along with minute differences in the chemical constitution. Furthermore, precise time course studies related to the downregulation of collagen I and ALP in a time-dependent manner and uncontrolled expression of Matrix metalloprotinase (MMP)s and osteocytic terminal differentiation markers may enable us to evaluate the *in vitro* results with the *in vivo* clinical outcome [28]. Despite being successful *in vitro*, maintenance of their long-term viability followed by pre-clinical testing concerning mechanical loading, strength, and the potential for osseointegration along the chances of graft rejection needs to be investigated.

Hence, the objective of the present study was to probe the *in vivo* osteogenic response to a 3D HAP scaffold printed by DWA in tibial defects in skeletally mature female Wistar rats. Tissue response due to the HAP scaffolds at the site of the tibial defect 12 weeks post-implantation was assessed by detailed histological analysis and micro-computed tomography (micro-CT). Although *in vivo* studies play a crucial role in testing a biomaterial, *in vitro* assays are critical in screening biomaterials with essential characteristics before evaluating more promising *in vivo* materials. Therefore, to answer whether the *in vitro* study we carried out previously served to pre-screen the HAP scaffold before implantation in the rat tibia, we conducted direct correlation studies between the results obtained *in vitro* and *in vivo* using Pearson's correlation coefficient. Taken together, our study reports the successful reconstruction of tibial defects in rats, which points to a new perspective for the use of custom-made 3D printed HAP structure to achieve a potential substitute for the healing of sub-critical size bone defects.

2. Materials and methods

2.1. HAP ink

The HAP powder ($Ca_{10}(PO_4)_6(OH)_2$) used in this study were procured from Sigma-Aldrich (99.9% purity) (Cat No. 12167-74-7). Details of all other reagents used were mentioned, along with the experimental methods. Printable HAP ink was prepared according to a previously described protocol [28]. Commercially available HAP particles were calcined at 1000 °C for 10 h, followed by ball milling at 100 rpm for 30 h to reduce the size of the HAP powder. A suspension was prepared by first dissolving the dispersant, sodium polyacrylic acid (Sigma-Aldrich, Cat No. 416029) solution in deionized water and adjusting the pH to 9.0 which was tuned with 5 M ammonium hydroxide and 1 M nitric acid. The HAP powder was then added to this suspension under constant stirring, followed by ultrasonication for 30 min, and the pH was adjusted to 9.0. The remaining HAP particles were added to the suspension, stirred again, followed by ultrasonication and pH adjustment. The suspension was stirred overnight at room temperature to ensure proper mixing. The following day, the suspension was filtered and centrifuged at 2000 rpm for 1 h. Next, 5 mg ml^{-1} carboxymethylcellulose (CMC) (Central Drug House, India, Cat. No. 027649) was added as a thickening agent. Finally, the HAP suspension was gelled by adding a 2 M $Ca(NO_3)_2$ (Cat. No. 22285) solution (0.05 ml to produce a concentrated HAP ink with the appropriate viscoelastic properties required for DWA.

2.2. Fabrication of scaffolds *via* DWA

The fabrication of self-supportive 3D periodic HAP scaffolds followed a methodology previously described [28]. HAP ink was extruded using a 260 m diameter stainless steel tip (Suzhou Lanbo Needle Co. Ltd, China) installed on a three-axis, computer-controlled robotic stage (Fiber Align, Aerotech Inc., Pittsburgh, USA) of DWA. The ink was injected into the syringe and placed in the DWA's barrel. For printing, a temperature of 25 °C was employed, and a pneumatic pressure of 25–30 psi was maintained for ink extrusion at a writing speed of 0.3 mm sec^{-1}, all controlled by customized software (3D Inks, Stillwater, OK, USA). A circular model with an overall set dimension of scaffolds in the range of 25 mm^2 in the *x-y* plane, a center-to-center spacing of 600 m, and seven consecutive layers were used for printing. Without breakdown, the HAP scaffolds were sintered at 1250 °C for densification. The scaffolds were heated at 1 °C min^{-1}–400 °C for 1 h, then at 3 °C min^{-1}–900 °C for 2 h, and then at 4 °C min^{-1} to the sintering temperature with a holding for 2 h.

2.3. Material HAP characterization

2.3.1. Micro-CT

3D printed HAP scaffolds with a bulk density of 1.605 g cm^{-3} were fabricated (measured geometrically). X-ray micro-CT (CT 50, Scanco Medical AG, Switzerland) was used to create 3D pictures of the HAP scaffolds, scanned at 70 kV, 114 A, and a voxel resolution of 10 m. Multiple images and slices ranging from 25 to 100 images were used to generate 3D morphometric calculations from in-house image analysis methods.

2.3.2. Dynamic light scattering (DLS) analysis

DLS analysis was used to determine the particle size distribution of HAP powder before and after ball milling. Analysis of the colloidal solution of HAP powder in ethanol was performed on Nano-ZS90 (Malvern), a United Kingdom instrument. A colloidal

solution of HAP powder in ethanol was prepared by dispersing a small amount of HAP powder (0.1 g) in 10 ml ethanol followed by ultrasonication for 15 min. Measurements were taken at a sampling time of 100 μs and 100 accumulations.

2.3.3. Energy-dispersive x-ray emission (EDX)

To confirm the material's elemental composition and validate it in terms of any existing impurities, EDX analysis of both powdered HAP and sintered scaffolds was performed on carbon-coated samples. A Zeiss EVO 50 high-definition Scanning Electron Micrscope (SEM) was used to image the samples, and the Ca/P ratios were calculated from the EDX spectrum.

2.4. Animal implantation surgeries

After printing within a UV sterilized 3D printed stage top, the HAP scaffolds were autoclaved before implantation.

2.4.1. Animal surgical procedures

All animal procedures were approved and orchestrated following the guidelines of the appropriate institutional (All India Institute of Medical Science, Delhi) animal care and ethical committee. In ten female Wistar rats (12 weeks old, 250–300 g body weight), a single 3 mm diameter sub-critical lesion in the medial side of the right tibia was created. An anaesthetic mixture of 2.0 ml Ketaset (100 mg ml^{-1}), 1.0 ml Xylapan (20 mg ml^{-1}), and 5 ml phosphate-buffered saline was administered into rats (PBS, pH 7.4). As soon as the animal had reached a deep plane of anesthesia, mechanical clippers were used to shave the lower right leg, and the area was cleared of fur by applying a depilatory cream. Next, moist gauze was used to wipe the leg, and three consecutive washes with chlorhexidine diacetate were used for disinfection (C6143-25G, Sigma-Aldrich, India) followed by 70% isopropanol. In addition, for palliative pain prevention, subcutaneous injection of 5 mg ml^{-1} meloxicam (Y0001080, Sigma-Aldrich, India) was given.

Above the middle third of the medial portion of the tibia, a full-thickness skin incision (1.5 cm) was created longitudinally. The skin flap was opened with fine spreaders, revealing the underlying tibia. The connective tissue on the tibial surface was removed, and a 3 mm circular defect was made using a trephine bur that extended down to the level of the marrow cavity. Suction was used to gently remove blood and bone pieces from the defect site, and saline irrigation was used to keep the tissue moist. Rats were randomly divided into two groups ($n = 5$) as follows: (a) HAP implanted and (b) controls with defect only (sham control). The implants were inserted into the defect with care. Following implantation, closed sutures were used to anchor the muscle, followed by a running suture for the skin flap. To prevent contamination of the operated site, animals were given a topical application of 0.2% chloramphenicol antibiotic solution to the sutured skin, followed by an intraperitoneal infusion of 5 ml of 5% dextrose-saline solution. Rats were kept in well-ventilated rooms with 12 h light: dark cycles and were given access to food and water ad libitum. After 12 weeks the animals were euthanized, their tibiae were harvested, and tissues were subsequently processed for micro-CT and histological analysis.

2.5. Post-harvest *ex vivo* analysis

2.5.1. Micro-CT analysis

Using high-resolution x-ray micro-CT (Scanco Medical, Switzerland), the development of new bone around the implanted scaffolds in relation to the rat tibial bone was determined. The scanning parameters for the tibiae were 70 kV, the intensity was 114 μA, and a voxel resolution of 10 μm $voxel^{-1}$. The samples were scanned with an optical fiber of known density to allow image intensity normalization. The parameters analyzed included bone mineral density (BMD), bone volume/tissue volume (BV/TV) ratio, trabecular thickness (Tb.Th.), Trabecular numbers (Tb.N.), and trabecular separation (Tb.Sp.). The 3D images of the scaffold–host bone were obtained using the software package ImageJ (Image Processing Language, Scanco Medical AG, Brüttisellen, Switzerland). Further, the noise and global fixed threshold of the gray-level images were Gaussian filtered (support 1, Sigma 1.2).

2.5.2. Histomorphometry

Formalin-fixed tibiae were decalcified for histology by immersing them in 14% disodium Ethylene diaminetetra acetic acid (EDTA) (Sigma–Aldrich, UK) at pH 9.0, with continual agitation at 5 rpm in a roller mixer at room temperature. The decalcification solution was changed three times a week for 14 days. The samples were then dehydrated in ethanol at increasing concentrations, cleared in xylene, and embedded in paraffin.

About 7 mm thick slices were cut, lifted onto slides (Superfrost slides; Thermo Scientific, India) precoated with 3-aminopropyl triethoxysilane (Sigma Aldrich, India), and stained with hematoxylin and eosin (H&E).

ImageJ program was used for histomorphometric analysis [29]. The unoperated right legs of rats without any defect and that of the implanted (right leg) were processed similarly to compute the standard medial wall diameter of the rat tibia.

Transverse histological sections were procured from the un-operated tibiae, stained with H&E, and examined using a fluorescence microscope (Leica DFC295, Germany) using Leica software application suite (LAS V3.8).

2.6. Statistical analysis

Each test was carried out in triplicates. Unless otherwise stated, data is provided as mean ± standard

deviation. Pearson's correlation was used to determine whether the *in vitro* and *in vivo* data had a significant linear relationship. The threshold for statistical significance was fixed at $p < 0.05$. The overall correlation was determined by scoring both the *in vitro* and *in vivo* outcomes for the same biomaterial on a scale of 1–5 (with 1 = poor and 5 = very good).

3. Results

The MCR 302 rheometer was used in a prior study [28] to analyze the rheology of printed HAP ink. AFM nanoindentation was used to measure the surface roughness and stiffness of the 3D printed HAP scaffold. SEM analysis was used to determine the morphological properties and microstructure of the sintered scaffold. The chemical characteristics of the sintered scaffolds were determined using XRD and ATR-FTIR. Overall, the findings suggest that our 3D printed HAP scaffold is well defined and suited for osteoblast to osteocyte differentiation [28].

3.1. Structural analysis

The particle size distributions of HAP powder before and after ball milling was determined by DLS, as shown in figures 1(a) and (b). The values of size distributions were found to be in the range of mean ± SD (figure 1(a)) and the mean ± SD (figure 1(b)) before and after ball milling, respectively. The average particle size was reduced to 220 nm from 963 nm within 30 h of ball milling, as shown in table 1. These results indicate the presence of agglomerations consisting of small-sized primary particles. These results are in good agreement with the SEM results previously reported by our group [28]. Moreover, EDX analysis indicated that only pure HAP, i.e. calcium and phosphate phase without any other impurity was present in commercially available powder samples and sintered 3D printed scaffold. The ratio of the concentration of calcium and phosphate were found to be 1.698 and 1.675 for the powder sample, and sintered 3D printed HAP scaffolds, respectively (table 1). These values are in good agreement with the stoichiometric value of the ideal HAP, which was reported to be 1.67.

Figure 1(c) shows the micro-CT image of the HAP scaffolds before implantation. An interconnected pore throughout the layers was conspicuous in this image. The BV/TV value was found to be 0.57 (figure 1(d)).

3.2. Clinical evaluation

No mortality occurred during or after surgery (figure 2). No signs of infection were detected after surgery. The animals were reported to feed normally; there were no reports of weight loss during the study, and their weight was based on the animals' size and age. The load-bearing ability of the experimental limb was found to have resumed, and the animals remained in good health throughout the study. No remarkable inflammatory reactions or implant failure was observed over the 12 weeks implantation period, and the defects were reported to have healed with complete closure and without scarring. Overall, no postoperative complications were observed.

3.3. Findings of micro-CT

Representative micro-CT images of the rat tibiae after 12 weeks of implantation are shown in figures 3(A) and (B). Analysis of morphometric parameters revealed that the implanted HAP scaffolds possessed a BMD value 61.5% higher than the sham control sites (figure 3(C)). The BMD of the tibia implanted with scaffolds was 1024 mgHA ccm^{-1}, which was very similar to that of the native tibia (1048 mgHA ccm^{-1}) (figure 3(C)). The unoperated or native tibia was scanned in the form of positive control, which displayed the full-thickness cortical bone in the ROI with a bone volume fraction (BV/TV) of 0.58. A reduced BV/TV value was observed in the sham control group ($p = 0.47$). In the characterization of trabecular bone, BV/TV represents an essential morphologic value. Interestingly, BV fraction was restored in the implant group (0.58). This suggests that most scaffold-implanted regions were deposited with HAP (figure 3(D)).

Tb.Th of the implanted scaffold was found to be 0.39 mm that was almost similar to that of the native tibia (0.40 mm); however, it got drastically reduced in the sham control (0.11 mm) (figure 3(E)). Hence, although healing was observed at the defect site of the sham control, the tibial wall diameter was reduced. Similarly, the connectivity density between the various trabeculae was much higher in the scaffold-implanted region than in the sham control, suggesting better interconnectivity and trabecular organization (data not shown). Moreover, the Tb.N was higher in the HAP-implanted region than in the defect-only condition, suggesting better connectivity and lesser coarseness than the control group (figure 3(F)). However, Tb.Sp was not significantly different between the HAP scaffold implanted and the positive control group (data not shown). Interestingly, the structure model index, which determines the rod-like geometry of trabecular structures, showed that the scaffold-implanted region was between 0 and 3, suggesting an intermediate value between the rod and plate-like trabecular structures similar to that of native bone. At the same time, it was significantly lower in the sham control, suggesting a more plate-like nature.

The medial wall diameter of the native tibia was 700 μm (figure 4(A)). After 12 weeks of the study period, the diameter of the sham control was reduced to 200 μm (figure 4(C)), on the other hand, an increase in medial wall diameter (875 μm) was

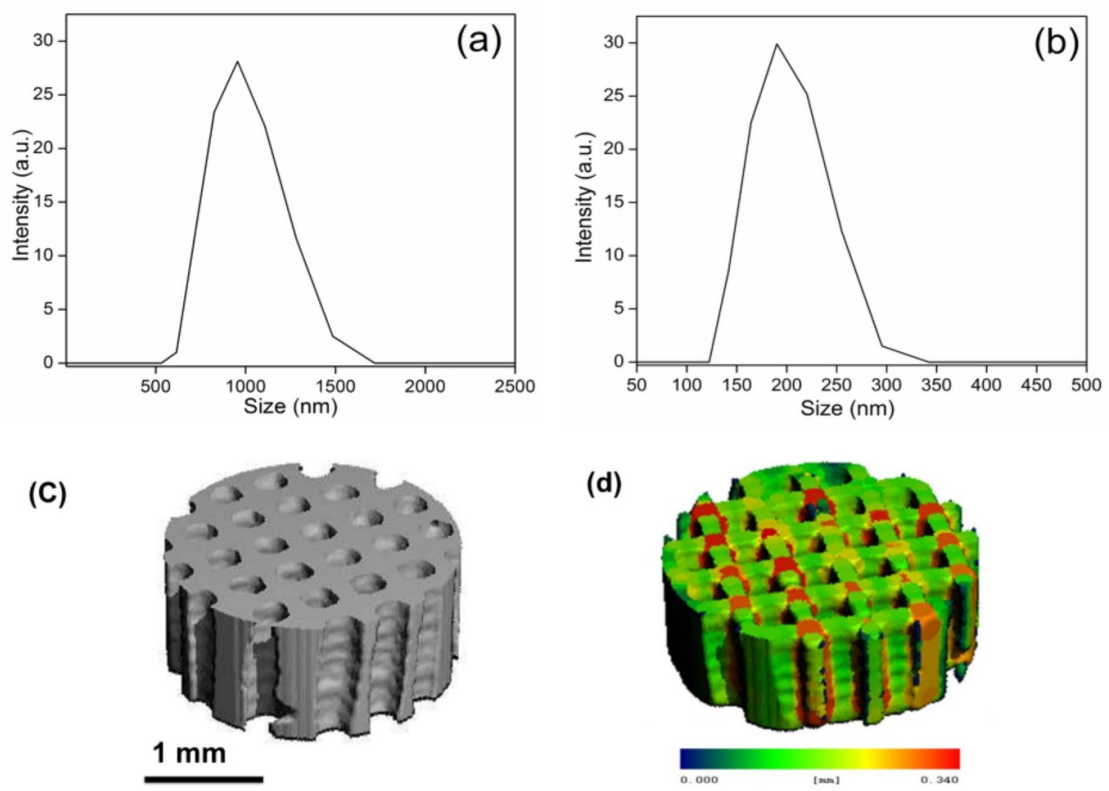

Figure 1. Particle size distribution (a) before (b) after ball milling for 30 h; (c) representative micro-CT image of HAP construct used for pre-clinical implantation in rat sub-critical sized 3 mm tibial defects; (d) the BV/TV value of the printed HAP scaffold was found to be 0.57.

Table 1. Characteristics of HAP powder and 3D scaffolds.

S. No.	Sample description		Average particle size (nm)	Ca/P ratio
1.	HAP powder	Before ball milling	963	1.698
		After ball milling	220	
2.	3D scaffold			1.675

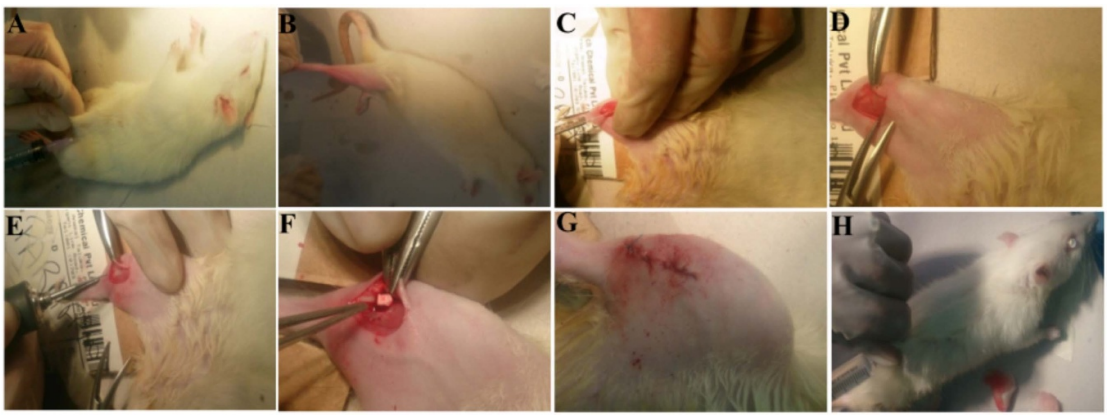

Figure 2. The surgical procedure involved in the preparation of the tibial defect and scaffold implantation into the defect site (A) female Wistar rats were injected with an anesthetic mixture; (B) lower right leg was shaved with mechanical clippers and was cleared of fur; (C) a full-thickness skin incision of 1.5 cm was made longitudinally above the middle third of the medial aspect of the tibia; (D) fine spreaders were used to open the resultant skin flap exposing the underlying tibia; (E) the tibial surface was cleared of connective tissue and a 3 mm circular defect was created using a trephine bur; (F) the HAP implant was gently inserted into the defect; (G) the muscle was secured in place by closed sutures followed by a running suture for the skin flap; (H) post-surgery, animals received topical application of 0.2% chloramphenicol antibiotic solution to the sutured skin to prevent contamination of the operated site.

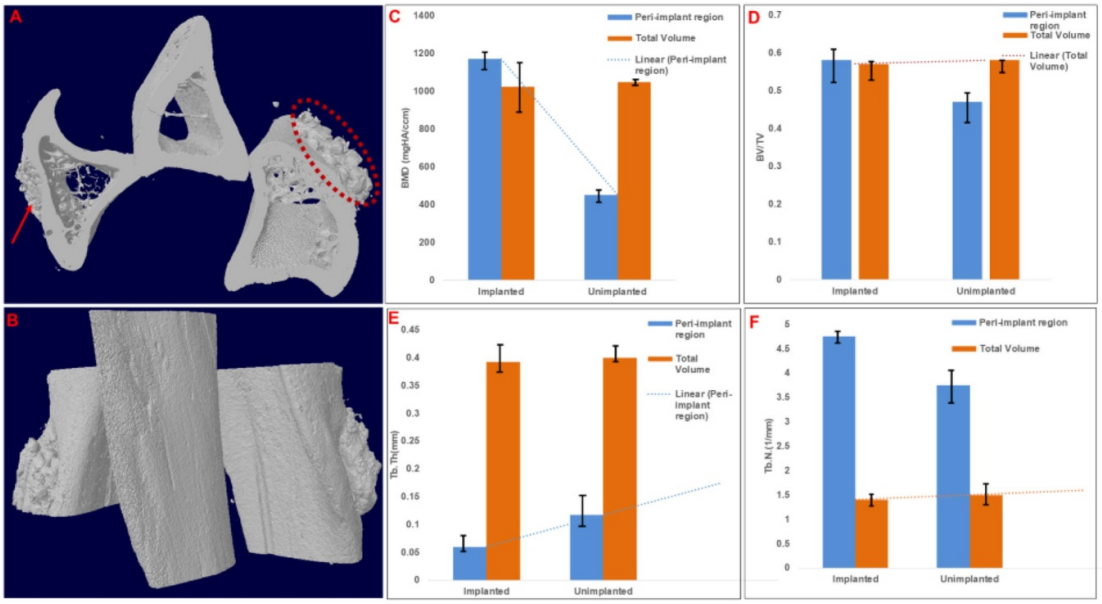

Figure 3. (A), (B) Micro-CT images showing 3D representative volume models (not to scale) denoting the transverse and longitudinal section of the rat tibia with different conditions, i.e. defect only, native tibia and tibia with the implant. The red arrow represents the defect area, whereas the dotted red circle represents the implanted HAP scaffold; (C) BMD calculations for the peri-implant region showing high HAP deposition in the peri-implant region of the implanted site as compared to sham control group (see trendline in peri-implant section). Similarly, overall mineral deposition is highly similar between scaffold implanted bone and native tibia (compare total volume series); (D) BV/TV ratio in the implant was identical to the native tibia. A decrease in the ratio was observed in the sham control. BV/TV of the total volume is comparable in the implanted and unimplanted groups indicative that bone formation is not compromised (see trendline in total volume series); (E) trabecular thickness resulting due to bone regeneration is nearly equal to the native tibia (see trendline in total volume series), and coarseness is lower in peri-implant region implanted with scaffold as compared to sham control region (see trendline in peri-implant region); (F) trabecular number is higher in the scaffold implanted group as compared to the defect site (compare peri-implant region series) and trabecular number is similar to the native tibia (see trendline in total volume series).

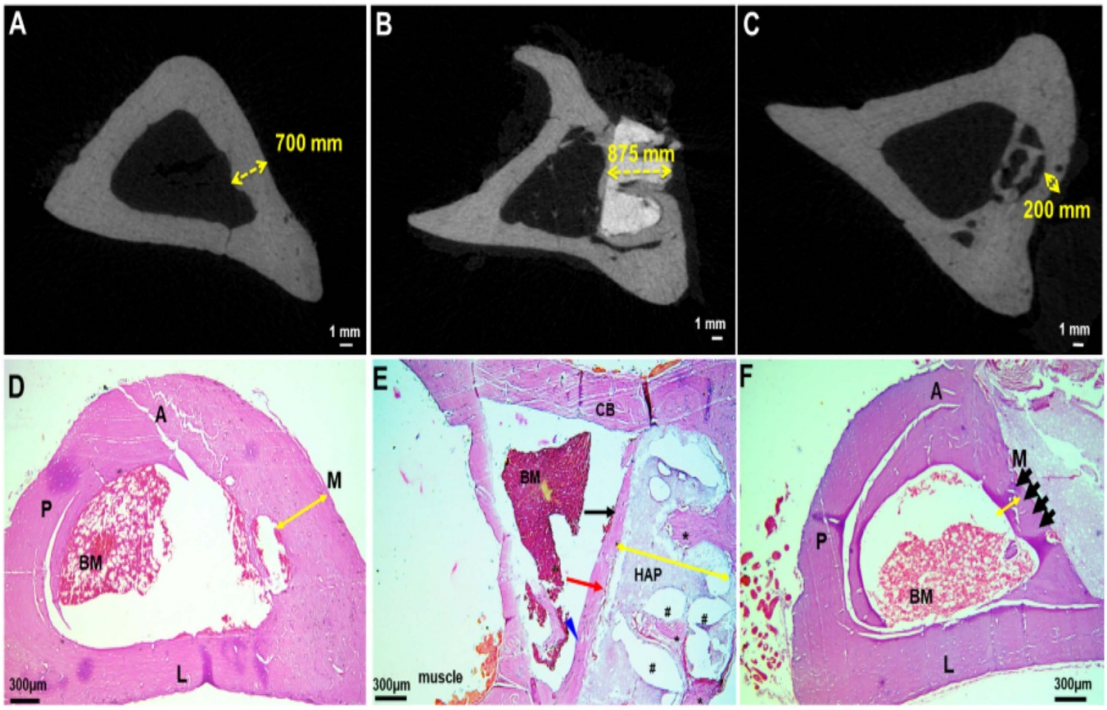

Figure 4. Representative micro-Ct images showing rat tibial bone at different conditions (A) unoperated bone; (B) with HAP implant; (C) defect only (sham control), 3 mm intramedullary rat tibial defect without the implant, after 12 weeks of healing closure of the defect with new bone (of similar density to the old bone as evident from similar gray-scale contrast) was evident, albeit the diameter of the medial wall was significantly (3.5 times) lesser.

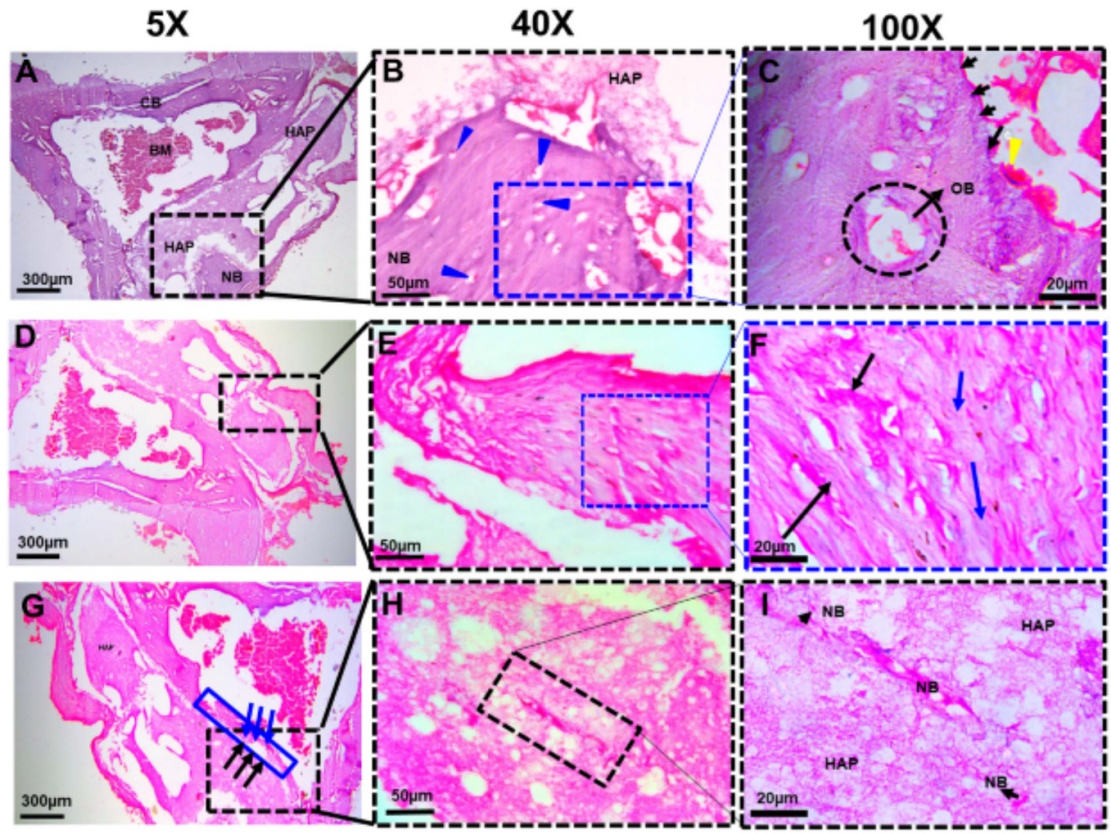

Figure 5. Histological images representing the 3D printed HAP scaffolds implanted into the medial side of rat tibia over 12 weeks (A) complete view of the transverse tibial section, where new bone (NB) ingrowth is seen into the hydroxyapatite (HAP) pores; (B) magnified view of (A), blue arrowheads display osteocytes; (C) magnified view of (B), the black circle shows the Haversian canal with connective tissue and blood vessel, black arrow shows osteoblast cell and the yellow arrowhead represents a multinucleated cell similar to the osteoclast; (E) magnified view of (D), showing vascularization of the newly formed bone; (F) magnified view of (E) where blue arrows represent the new bone and black arrows represent vasculature; (G) blue rectangle shows the interface between the old bone (blue arrow) and the HAP implant (black arrows); (H) magnified view of (G) showing the HAP implant; (I) magnified view of (H) showing the formation of new bone within the HAP pores.

observed in the case of the tibia with the HAP implant (figure 4(B)). Moreover, trabecular bone formation was observed in the tibia of the HAP implant.

3.4. Histomorphometry

The results obtained from H&E staining 12 weeks post-implantation corroborate the findings of micro-CT. It is clear from the images that the HAP implants were seamlessly integrated into the site of the bone defect in a manner such that it became difficult to differentiate it from the surrounding bone. This indicates the absence of conspicuous inflammation and foreign body reactions (figure 4(E)). New bone formation was observed along the margins of the defect (figure 5(A)), which exhibited morphological features similar to those of the surrounding mature bone, including some organized osteocytes (figure 5(B)). As shown in figure 5(C), some osteoblastic proliferation was observed along the newly formed bone in the implant group (figure 5(B)) and a Haversian canal containing connective tissue and blood vessels (figure 5(C)). A cluster of multinucleated cells was found in the vicinity of the newly formed bone and the implant in a different section ($n = 6$) exhibiting osteoclastic morphology (figure 5(C)). Numerous blood vessels were also observed in the newly formed bone penetrating the HAP pores (figure 5(F)). Interestingly, the osteoblast population initiated new bone formation, which helped fill the porous structure of the 3D HAP.

On the other hand, the sham control rats with only empty defects manifested the formation of new bone, whose density was morphologically similar to the surrounding cortical bone. It was challenging to identify the defect margins due to the operated site's absolute osseous fusion (figure 4(F)). There was no sign of inflammation akin to the rats with the HAP implant. However, a reduction in medial wall diameter was conspicuous (figure 4(F)) compared to the native rat tibia (figure 4(D)). Few osteocytic movements were observed around the newly formed bone, which indicates the formation of mature bone and calcium deposition similar to that present in the native bone (figure 6(F)). A thin fibrous tissue formation was observed adjacent to the defect site (figure 6(A)).

Light micrographs of H and E-stained transverse sections from the (D) native rat tibia. The double-headed yellow arrow represents the diameter

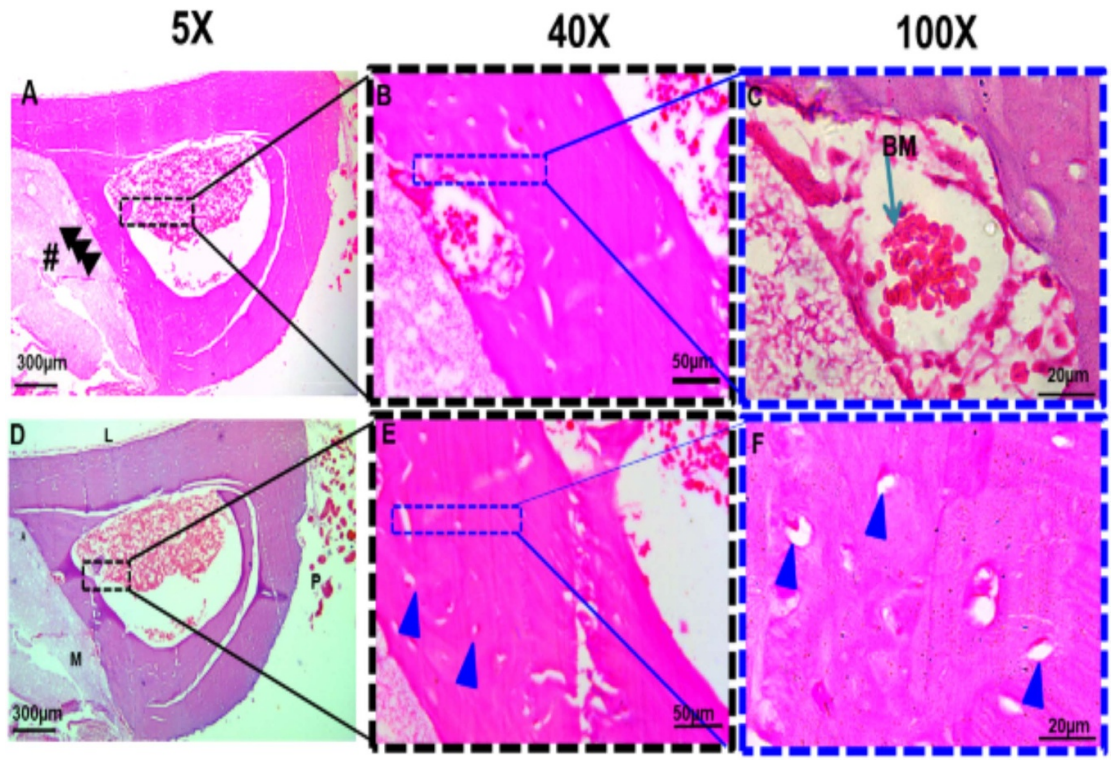

Figure 6. Histological images representing the sham control over 12 weeks (A) a complete view of the transverse tibial section where complete bony union have occurred, black arrows represent the defect site, '#' shows the fibrous matrix formed adjacent to the defect; (B) magnified view of (A); (C) magnified view of (B), bone marrow (BM) is formed at the vicinity of the defect; (E) magnified view of (D), blue arrowheads show the osteocytes; (F) blue arrowhead represents osteocytes, where L-lateral, A-anterior, M-medial, P-posterior, blue arrow-bone marrow.

Table 2. Parameters and their corresponding scores for correlation.

In vitro parameters	Scores	*In vivo* parameters	Scores
Alkaline phosphatase (ALP) assay	4 4 5	BMD values (micro-CT)	4 5 5
Mineralization assay (alizarin red staining)	3 2 3	BMD values (micro-CT)	4 5 5
Gene expression (osteoblast marker)	5 4 4 3 4 5	Osteoblast proliferation (histology)	3 2 2 2 1 2

of the medial wall; (E) tibia with the HAP implant, where new bone ingrowth is observed in the HAP surface and inside HAP pores (*), '#' shows the HAP artifacts, black arrow represents an osteocytic morphology, the red arrow shows the operation of the medial wall, and the blue arrowhead represents cortical bone-like morphology, the yellow arrow represents the increased diameter of the medial wall, and; (F) sham control group that displays complete union of the bone defect represented by black arrows; however, there is a reduction in the medial wall diameter (yellow double-headed arrow). The detachment of the bone marrow from the tibial wall is a processing artifact. Abbreviations: A-anterior, P-posterior, M-medial, L-lateral, HAP-hydroxyapatite, CB-cortical bone, BM-bone marrow.

3.5. *In vitro* and *in vivo* parameters assessed for correlation

In vitro analysis of our developed HAP scaffold was carried out as described in our previous study [28]. Of the results obtained from our earlier and the present study, the sets of *in vitro* and *in vivo* parameters used to assess correlation and their corresponding scores are shown in table 2, which were used to correlate this predictive outcome.

Null hypothesis: Existence of no correlation between the *in vivo* and *in vitro* results

Hypothesis: Specific *in vitro* parameters can be utilized to predict the results related to the material *in vivo*.

Upon calculating Pearson's correlation, the value of the coefficient of correlation (r) was found to be 0.420 between the results of gene expression and histology, which is an indication of a positive correlation between the two (figure 7(A)). A similar correlation was found with an (r) value of 0.5 between the ALP and BMD values from micro-CT (figure 7(B)). However, a contrasting result was obtained by correlating the alizarin assay with BMD. Instead of a positive correlation, a negative (r) value was obtained, i.e.−0.5 (figure 7(C)).

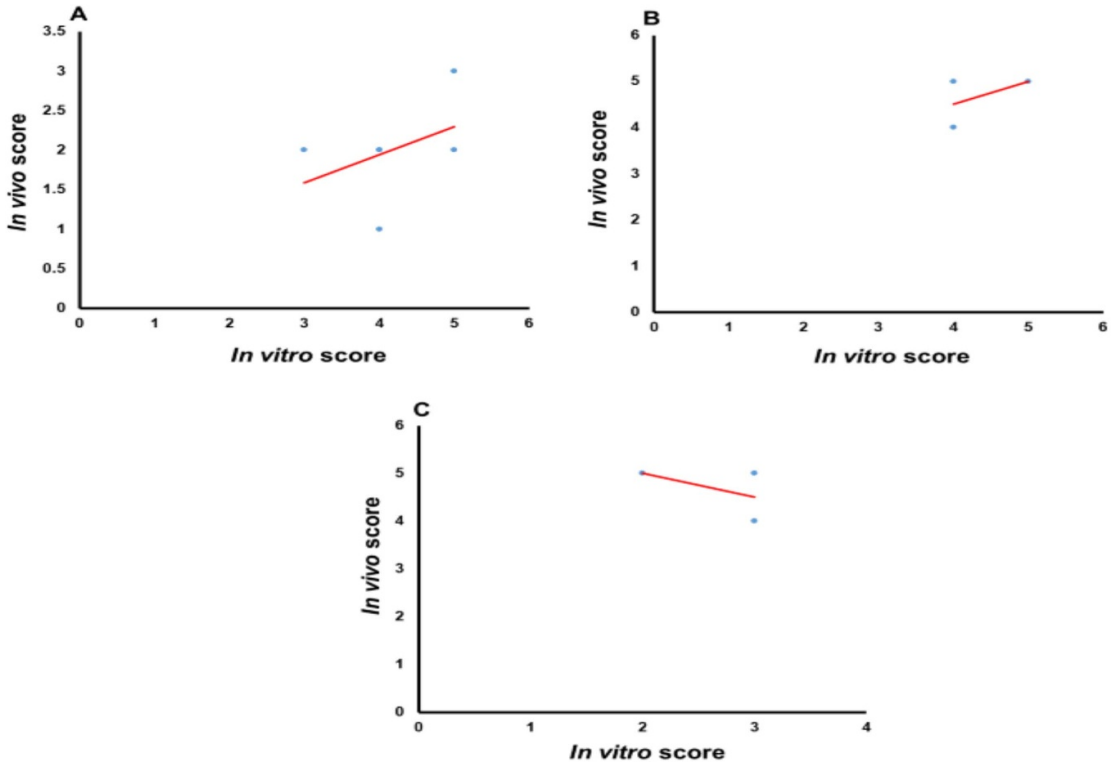

Figure 7. Pearson's correlation between the *in vitro* and *in vivo* parameters testing the HAP biomaterial (A) correlation between gene expression (*in vitro*) and histology, i.e. H and E staining (*in vivo*); (B) correlation between ALP assay (*in vitro*) and BMD from micro-CT (*in vivo*); (C) correlation between Alizarin red assay (*in vitro*) and BMD from micro-CT (*in vivo*).

4. Discussion

Conventionally used HAP powder used for filling bone defects [30] are limited by several factors, such as their inability to be used for load-bearing orthopedic implants because of the diminished mechanical properties and the ability of the powder to migrate to neighboring areas. These limitations were overcome using HAP blocks [31]. However, these blocks had to be reshaped intraoperatively by the clinicians, which would sometimes result in scaffolds unsuitable for implantation. The absence of pores does not allow the migration of nearby osteoblast cells to the defect site. In that respect, 3D printing of HAP scaffolds by DWA helped us overcome these drawbacks and provide a porous matrix that persuaded the migration and proliferation of osteoprogenitor cells, resulting in the formation of a mineralized matrix around the implant. The printed 3D HAP scaffolds were composed of calcium and phosphate, that is, HAP without any impurities, as confirmed from the EDX analysis that was used to determine the uniformity of the scaffolds. The ratio of calcium to phosphate complied with the ideal HAP ratio, as shown in table 1. These results indicate that our prepared 3D printed scaffold would be a potent material for bone regeneration in critical-size bone defects. Moreover, the physical characterization studies carried out in terms of FTIR, SEM, AFM, and XRD previously [28] demonstrated that our 3D printed HAP construct is a highly reactive and appropriate scaffold that supports the differentiation of osteoblasts to osteocytes. Although several studies have reported 3D printing of HAP scaffolds, for example Cox *et al* 3D printed HAP along with poly(vinyl)alcohol powder [32], our printed scaffold advantage was that it had been used to study the rat tibial defects *in vivo* not carried out in the previous studies.

The ink prepared in this study exhibited shear thinning behavior, indicating that our prepared ink is appropriate for fabricating suitable scaffolds by DWA without undergoing any deformation [28]. In a similar study, Michna *et al* formulated a concentrated HAP ink with suitable viscoelastic properties appropriate for the fabrication of multiscale porous 3D periodic scaffolds via DWA [22]. There was an uninterrupted extrusion of the ink in filaments to produce the required scaffold framework in a layer-by-layer manner. Moreover, the scaffolds could be heated abruptly after drying due to fewer organic species in the formulated ink. Although this group was successful in preparing HAP scaffolds with high print fidelity and interconnected macropores, the ink prepared by us was advantageous in comparison to them because of the employment of a cellulosic derivative (CMC) that acts as a thickening agent as well as a viscosity modifier that improves the printability [33]. Furthermore, sonication carried out for a longer period aided

in homogenous dispersion and disintegration of the HAP particles, which was in agreement with the results obtained by DLS.

We focused on three conditions: (a) the HAP implant into the tibial region, (b) the only defect area without any implant (sham control), and (c) the native tibia (positive control). Self-healing was conspicuous in the sham control group; however, there was a drastic reduction in the tibial wall thickness. Gross examinations of the animals that underwent surgery were carried out either visually or by a stereomicroscope throughout the 12 weeks of the study period, which did not show any signs of inflammation, degeneration, or osteolysis. The repair and formation of new bone at the defect site were assessed by micro-CT quantitatively and qualitatively by histomorphometry 12 weeks post-implantation. Higher BMD values of the defect site where HAP scaffolds were implanted than those for the sham defect sites suggested successful integration and extensive mineralization in the scaffold-implanted area compared to the sham control.

Similarly, the BMD of the tibia implanted with scaffolds was very similar to that of the native tibia, suggesting that implantation of scaffolds successfully restored the mineral content. On the other hand, the BV fraction in the tibia implanted with scaffolds was comparable to that of the native tibia, suggesting that most of the scaffold-implanted region was deposited with HAP, which indicates that the regenerated tissue possesses native tissue-like mechanical and tensile properties. A higher number of trabeculae with Tb.Th and significantly better interconnectivity between the individual trabeculae in the implant group than in the native bone suggests that the implantation of HAP scaffolds successfully led to the regeneration of a native bone-like structure. However, Tb.Sp was not significantly different between the HAP scaffold implanted and the positive control group. Analysis of bone morphometry parameters suggested that implantation of the HAP scaffold resulted in the regeneration of bone tissue with native bone-like properties. In a similar study with 3D periodic HAP scaffolds, Simon *et al* reported a consistent and extensive bone formation in the calvarial defect of skeletally mature rabbits that was about 63.5%–95.5% at the end of 16 weeks [34]. Higher BMD values in the case of implanted compared to the sham control indicate bone formation in the defect site due to the stimulatory activity of calcium and phosphate ions released slowly with time during material degradation. However, it should be noted that bone outgrowth from the surface of the tibia is due to surgery, which might not have been carried out properly.

Histological analysis showed an augmentation in the BV within the implanted HAP scaffold, which corroborates the findings of micro-CT. The histological findings confirmed seamless integration of the HAP scaffold at the defect site. This correlates with our earlier findings in different *in vitro* studies, where 3D HAP scaffolds exhibited increased osteoblastic and osteocytic differentiation. These scaffolds persuaded the cells to grow optimally *in vitro* on their surface and into the pores, mimicking the native bone-like architecture [28]. Positive confirmation from the results obtained from 3D HAP carried out *in vitro* prompted us to investigate its role and application in *an in vivo* rat tibial model. Interestingly, new bone ingrowth was conspicuous at the HAP surface and within its pores when the scaffolds were implanted *in vivo*, as observed in the H&E studies. The presence of scattered osteoblasts at the newly formed bone site and associated osteocytes concurs with the results obtained *in vitro*. The culturing of osteoblasts on 3D HAP *in vitro* resulted in a substantial filamentous structure mimicking the osteocyte ultrastructure around the 6th week, supporting our *in vivo* findings [28]. Gene expression analysis of the osteoblasts seeded in the 3D HAP scaffold revealed the upregulation of the osteoblast marker with defined early, mid, and late-stage osteoblastic maturation in a time-dependent manner, along with alkaline phosphatase and uncontrolled expression of matrix metalloproteinase has been observed. ALP and RunX2, markers of early osteogenesis, were expressed abundantly in 3D HAP scaffolds *in vitro*, indicating ordered and superior bone formation. An enhanced podoplanin expression evidenced osteocytic differentiation in the 4th week and sclerostin in the 6th week. These *in vitro* findings justified the osteogenesis of the HAP scaffolds when implanted in tibial defects. The appearance of osteoclasts at the interface between the implant and the new bone indicates that bone resorption occurred. The new bone started substituting the implant, and mineralization took place at the new bone site. A homogeneous amount of tissue within the pores of the scaffold indicates that the internal pores within the scaffold facilitate similar ingress to the cells and tissues.

The reproducibility of our study was evaluated by comparing it to that of the controls. Sham control corresponds to the empty defect, although it showed a complete bony union with the surrounding cortical tissue such that the location of the newly formed tissue could not be differentiated from the defect area. However, it could fill only 38% of the defect volume with the mineralized matrix, as evident from the micro-CT analysis (BMD values). A thin fibrous matrix was formed adjacent to the medial wall where the defect was created. However, pronounced ectopic bone formation was observed in the implant group compared to the control group. Similar results were obtained by Choi *et al* [35] while implanting BMP-2/BCP (bone morphogenic protein 2/biphasic calcium phosphate) granules in the rabbit defect model, resulting in higher bone formation in the implant group compared to the defect which contained BCP

substitute in the absence of any coating that served as a control. It is interesting to note that although the defect of the sham control showed self-healing with reduced medial wall diameter compared to the positive control, it was ineffective for load-bearing purposes. Massive mineralization at the HAP implant site as visible via micro-CT and histology is convincing evidence that the sub-critical defect healed after implanting the HAP scaffold, which is suitable for load-bearing defects. This can serve as a blessing, where a ready-made patient and defect-specific scaffolds can be directly implanted into patients with any critical size defects, thus reducing the time and increasing the healing efficiency compared to the scaffolds where cells are seeded externally and then implanted into the patients.

Previous studies have reported that the biomimetic properties of HAP induce adequate osteoconductive properties at the implant area, signifying that rapid bone growth can be achieved by mimicking the native environment [36]. An increase in mineralization and osteoblastic activity has been observed while investigating the surface morphology [37–39] of biomimetic implants both *in vivo* and *in vitro*. However, these studies stressed modifying the scaffold surface morphology, such as by employing simulated body fluid [37] or by thermal phase separation technique [38, 39]. The results obtained from these studies indicate that replicating the native bone environment enhances the formation of new bone. This is in accordance with the findings of our study, which can be considered an addition to the previously mentioned studies, that 3D printed macroporous HAP scaffolds with biomimetic properties also promote new bone formation. Enhanced bone ingrowth into the scaffold is advantageous as adequate bone ingrowth is a prerequisite for providing perpetual support to the tissue-engineered scaffold and the regeneration of the bone tissue [40].

We directly correlated the *in vitro* and *in vivo* results using the same biomaterial to determine the interrelationship from previously performed experiments. Few studies have attempted to correlate histology and micro-CT-based mineralization [41]. The positive correlation obtained between the gene expression and histology and the ALP assay and BMD values from micro-CT indicates that our printed scaffolds support osteogenesis *in vitro* and are also suitable for implantation *in vivo*. However, there are a few reasons for a negative correlation between the Alizarin red assay and BMD values from micro-CT. First, the estimation of mineralization by alizarin red staining was 2D analysis, so it provided limited information about the organization of the mineralized matrix; however, the conditions *in vivo* are 3D. Second, only one type of cell was used *in vitro* for six weeks in the presence of externally added osteogenic components and selective growth factors, such as dexamethasone. However, many growth factors and multiple cell types such as stem cells and osteoblasts are involved in osteogenesis *in vivo*. In a previous study, Bara *et al* [42] reported the variation observed upon expansion between naïve MSCs and those cultured *in vitro*. The cited reason for this is that, due to the variation upon isolation and culture of the MSCs, culture protocols differing in density media and centrifugation steps resulted in a negative outcome during the *in vivo* clinical trial.

Following successful implantation of the HAP scaffolds *in vivo* in the rat tibial model, we extended our objective to target the 3D printed HAP constructs for human clinical application. An ongoing study is being conducted in parallel in our laboratory where the HAP scaffolds have been modified in the form of a tray for patients suffering from ameloblastoma to restore mandibular defects. This custom-made HAP tray would be helpful for oral and maxillofacial rehabilitation.

Taken together, our 3D printed HAP scaffold unlike the conventional scaffolds, exhibited excellent bone-like remodeling properties at the defect site, including bone mineralization by osteoblasts and resorption by osteoclasts. However, the major limitation of the present study is that we used a small rat tibial sub-critical defect model, whereas a substantial volume of graft material was applied to the defect area. Moreover, the experimental study period of 12 weeks was insufficient to compare the formation of new bone between the implanted and control groups with respect to both quality and architecture. To eliminate the bias of *in vitro* and *in vivo* results, a well-directed *in vivo* study and its future clinical application are the most priority research in our laboratory. Therefore, in subsequent studies, the ability of the 3D printed HAP scaffold could be elucidated for bone augmentation in more significant defects or for use in human clinical trials.

5. Conclusion

This study elucidated the application of 3D printed HAP scaffolds as a substitute for sub-critical size bone defects. Our printed scaffold was precise dimensionally and stable enough for *in vivo* implantation. The beauty of our developed scaffold was that it could be fabricated as per our requirement; hence, it is not only specific but also patient-specific, allowing us to print the required dimensions from the details obtained from preoperative CT scans. Altogether, the results obtained from our study indicate a positive correlation between the *in vitro* and *in vivo* outcomes. Pore size and pore interconnectivity play a vital role in osteoconduction. This aids in new bone formation and facilitates cell adhesion and efficient vascularization. This study highlighted that our 3D printed scaffold could boost neo-bone formation remarkably. Interestingly, the

developed HAP scaffold can diminish the dependency on allografts and autografts for bone repair, thus decreasing the surgery time, thereby influencing the overall result of the surgery and decreasing the related costs.

Data availability statement

The data that support the findings of this study are openly available at the following URL/DOI: Will be available when asked.

Acknowledgment

J C is grateful to the Department of Science and Technology (DST) for the Inspire Fellowship (SRF) No. IF160365, India. We would like to thank Dr Swati Midha and Dr Shikha Chawla for their help with animal surgery. We would like to thank Prof Amitabha Bandyopadhyay, IIT Kanpur for his help in MicroCT analysis.

Conflict of interest

The authors declare no conflict of interest.

ORCID iD

Sourabh Ghosh https://orcid.org/0000-0002-1091-9614

References

[1] Midha S, Tripathi R, Geng H, Lee P D and Ghosh S 2016 Elucidation of differential mineralisation on native and regenerated silk matrices *Mater. Sci. Eng.* C **68** 663–74
[2] Midha S, Murab S and Ghosh S 2016 Osteogenic signaling on silk-based matrices *Biomaterials* **97** 133–53
[3] García-Gareta E, Coathup M J and Blunn G W 2015 Osteoinduction of bone grafting materials for bone repair and regeneration *Bone* **81** 112–21
[4] Hulsart-Billström G *et al* 2016 A surprisingly poor correlation between *in vitro* and *in vivo* testing of biomaterials for bone regeneration: results of a multicentre analysis *Eur. Cell Mater.* **31** 312–22
[5] Chawla S, Sharma A, Bandyopadhyay A and Ghosh S 2018 Developmental biology-inspired strategies to engineer 3D bioprinted bone construct *ACS Biomater. Sci. Eng.* **4** 3545–60
[6] Sen M K and Miclau T 2007 Autologous iliac crest bone graft: should it still be the gold standard for treating nonunions? *Injury* **38** S75–S80
[7] Arrington E D, Smith W J, Chambers H G, Bucknell A L and Davino N A 1996 Complications of iliac crest bone graft harvesting *Clin. Orthop. Relat. Res.* **329** 300–9
[8] Banwart J C, Asher M A and Hassanein R S 1995 Iliac crest bone graft harvest donor site morbidity. A statistical evaluation *Spine* **20** 1055–60
[9] Greenwald A S, Boden S D, Goldberg V M, Khan Y, Laurencin C T and Rosier R N 2001 Bone-graft substitutes: facts, fictions, and applications *J. Bone Joint Surg.* A **83** 98–103
[10] Goodman S B 2007 Wear particles, periprosthetic osteolysis and the immune system *Biomaterials* **28** 5044–8
[11] Midha S, Kumar S, Sharma A, Kaur K, Shi X, Naruphontjirakul P, Jones J R and Ghosh S 2018 Silk fibroin-bioactive glass based advanced biomaterials: towards patient-specific bone grafts *Biomed. Mater.* **13** 055012
[12] Boskey A L and Roy R 2008 Cell culture systems for studies of bone and tooth mineralization *Chem. Rev.* **108** 4716–33
[13] Boskey A L 2015 Bone composition: relationship to bone fragility and anti-osteoporotic drug effects *BoneKEy Rep.* **4** 710
[14] Karageorgiou V and Kaplan D 2005 Porosity of 3D biomaterial scaffolds and osteogenesis *Biomaterials* **26** 5474–91
[15] Bohner M, Galea L and Doebelin N 2012 Calcium phosphate bone graft substitutes: failures and hopes *J. Eur. Ceram. Soc.* **32** 2663–71
[16] Otsuki B, Takemoto M, Fujibayashi S, Neo M, Kokubo T and Nakamura T 2006 Pore throat size and connectivity determine bone and tissue ingrowth into porous implants: three-dimensional micro-CT based structural analyses of porous bioactive titanium implants *Biomaterials* **27** 5892–900
[17] Bose S and Tarafder S 2012 Calcium phosphate ceramic systems in growth factor and drug delivery for bone tissue engineering: a review *Acta Biomater.* **8** 1401–21
[18] Gbureck U, Hölzel T, Klammert U, Würzler K, Müller F A and Barralet J E 2007 Resorbable dicalcium phosphate bone substitutes prepared by 3D powder printing *Adv. Funct. Mater.* **17** 3940–5
[19] Prakasam M, Locs J, Salma-Ancane K, Loca D, Largeteau A and Berzina-Cimdina L 2015 Fabrication, properties and applications of dense hydroxyapatite: a review *J. Funct. Biomater.* **6** 1099–140
[20] Song X, Tetik H, Jirakittsonthon T, Parandoush P, Yang G, Lee D, Ryu S, Lei S, Weiss M L and Lin D 2018 Biomimetic 3D printing of hierarchical and interconnected porous hydroxyapatite structures with high mechanical strength for bone cell culture *Adv. Eng. Mater.* **21** 1800678
[21] Chen S, Shi Y, Luo Y and Ma J 2019 Layer-by-layer coated porous 3D printed hydroxyapatite composite scaffolds for controlled drug delivery *Colloids Surf.* B **179** 121–7
[22] Michna S, Wu W and Lewis J A 2005 Concentrated hydroxyapatite inks for direct-write assembly of 3D periodic scaffolds *Biomaterials* **179** 121–7
[23] Sun L, Parker S T, Syoji D, Wang X, Lewis J A and Kaplan D L 2012 Direct-write assembly of 3D Silk/hydroxyapatite scaffolds for bone co-cultures *Adv. Healthcare Mater.* **1** 729–35
[24] Kolambkar Y M, Dupont K M, Boerckel J D, Huebsch N, Mooney D J, Hutmacher D W and Guldberg R E 2011 An alginate-based hybrid system for growth factor delivery in the functional repair of large bone defects *Biomaterials* **32** 65–74
[25] Schofer M D *et al* 2011 Electrospun plla nanofiber scaffolds and their use in combination with bmp-2 for reconstruction of bone defects *PLoS One* **6** e25462
[26] Vedakumari W S, Priya V M and Sastry T P 2014 Deposition of superparamagnetic nanohydroxyapatite on iron-fibrin substrates: preparation, characterization, cytocompatibility and bioactivity studies *Colloids Surf.* B **120** 208–14
[27] Martinelli N M, Ribeiro M J G, Ricci R, Marques M A, Lobo A O and Marciano F R 2018 *In vitro* osteogenesis stimulation via nano-hydroxyapatite/carbon nanotube thin films on biomedical stainless steel *Materials* **11** 1555
[28] Kaur K, Das S and Ghosh S 2019 Regulation of human osteoblast-to-osteocyte differentiation by direct-write 3D microperiodic hydroxyapatite scaffolds *ACS Omega* **4** 1504–15
[29] Schneider C A, Rasband W S and Eliceiri K W 2012 NIH image to imageJ: 25 years of image analysis *Nat. Methods* **9** 671–5

[30] Benezra Rosen V, Hobbs L W and Spector M 2002 The ultrastructure of anorganic bovine bone and selected synthetic hyroxyapatites used as bone graft substitute materials *Biomaterials* **23** 921–8
[31] Fujita R, Yokoyama A, Kawasaki T and Kohgo T 2003 Bone augmentation osteogenesis using hydroxyapatite and β-tricalcium phosphate blocks *J. Oral Maxillofac. Surg.* **61** 1045–53
[32] Cox S C, Thornby J A, Gibbons G J, Williams M A and Mallick K K 2015 3D printing of porous hydroxyapatite scaffolds intended for use in bone tissue engineering applications *Mater. Sci. Eng.* C **47** 237–47
[33] Mulakkal M C, Trask R S, Ting V P and Seddon A M 2018 Responsive cellulose-hydrogel composite ink for 4D printing *Mater. Des.* **160** 108–18
[34] Simon J L, Michna S, Lewis J A, Rekow E D, Thompson V P, Smay J E, Yampolsky A, Parsons J R and Ricci J L 2007 *In vivo* bone response to 3D periodic hydroxyapatite scaffolds assembled by direct ink writing *J. Biomed. Mater. Res.* A **83** 747–58
[35] Choi H, Park N J, Jamiyandorj O, Choi K H, Hong M H, Oh S, Park Y B and Kim S 2012 Improvement of osteogenic potential of biphasic calcium phosphate bone substitute coated with two concentrations of expressed recombinant human bone morphogenetic protein 2 *J. Periodontal Implant Sci.* **49** 114–26
[36] Wang H, Li Y, Zuo Y, Li J, Ma S and Cheng L 2007 Biocompatibility and osteogenesis of biomimetic nano-hydroxyapatite/polyamide composite scaffolds for bone tissue engineering *Biomaterials* **28** 3338–48
[37] Fan H, Ikoma T, Tanaka J and Zhang X 2007 Surface structural biomimetics and the osteoinduction of calcium phosphate biomaterials *J. Nanosci. Nanotechnol.* **7** 808–13
[38] Woo K M, Jun J H, Chen V J, Seo J, Baek J H, Ryoo H M, Kim G S, Somerman M J and Ma P X 2007 Nano-fibrous scaffolding promotes osteoblast differentiation and biomineralization *Biomaterials* **28** 335–43
[39] Chen V J, Smith L A and Ma P X 2006 Bone regeneration on computer-designed nano-fibrous scaffolds *Biomaterials* **27** 3973–9
[40] Cheung H Y, Lau K T, Lu T P and Hui D 2007 A critical review on polymer-based bio-engineered materials for scaffold development *Composites* B **8** 291–300
[41] Cowan C M, Aghaloo T, Y-f C, Walder B, Zhang X, Soo C, Ting K and Wu B 2007 MicroCT evaluation of three-dimensional mineralization in response to BMP-2 doses *in vitro* and in critical sized rat calvarial defects *Tissue Eng.* **13** 501–12
[42] Bara J J, Richards R G, Alini M and Stoddart M J 2014 Concise review: bone marrow-derived mesenchymal stem cells change phenotype following *in vitro* culture: implications for basic research and the clinic *Stem Cells* **32** 1713–23